Lateral GeSn Waveguide-based Homojunction Phototransistor for Next-Generation 2000nm Communication and Sensing Applications

1. Harshvardhan Kumar
The LNM Institute of Information Technology, Electronics and Communication Engineering Rupa ki Nangal, Post-Sumel, Via, Jamdoli JAIPUR, RAJASTHAN, IN 302031
Email: harshvardhan.kumar@lnmiit.ac.in
2. Qimiao Chen
Nanyang Technological University, School of Electrical and Electronic Engineering 50 Nanyang Avenue Singapore, SG 639798
3. Chuan Seng Tan
Nanyang Technological University, School of Electrical and Electronic Engineering 50 Nanyang Avenue Singapore 639798 REPUBLIC OF SINGAPORE, Singapore, SG 639671 92264667

Received xxxxxx
Accepted for publication xxxxxx
Published xxxxxx

Abstract

This work reports a novel mid-infrared (MIR) lateral $Ge_{1-x}Sn_x$ (x = 6%) waveguide-based phototransistors (PTs) on a silicon platform. A lateral device structure is proposed to enhance the optical confinement factor (OCF) and the optical power through the *i*-GeSn waveguide, thereby, increasing the optical responsivity of the PTs. The proposed devices are investigated using multiphysics simulation. The designed PTs are investigated in terms of the Gummel and output characteristics under both dark and illumination, 3dB bandwidth, optical gain, and responsivity. The effect of lateral scaling on various figure-of-merits of PTs is also studied and in return, helps optimize the device structure to get the highest optical gain, responsivity, and 3-dB bandwidth at 2000 nm. The theoretically optimized PT achieves the maximum optical gain of 1650 and responsivity of about 308A/W at 2000 nm, with $V_{BE} = 0.3V$ and $V_{CE} = 1\ V$. In addition, the device exhibits a record-high 3-dB bandwidth of >55GHz. Thus, the encouraging electrical and optical performance of the proposed PT manifests it as a great potential candidate for the 2000 nm band.

Keywords: Si-photonics, Phototransistor, GeSn, Photodetector

1. Introduction

With the ever-increasing requirement for high-speed fiber-optic telecommunications and mid-infrared (MIR, 1.8-5μm[1]) sensing and imaging applications, electronic and photonic integrated circuit (EPIC) platforms are being optimized to enhance the performance of optical detectors/sensors. The 2000 nm wavelength band has various potential applications, especially the next-generation fiber-optic communication, atmospheric gas sensing (CO_2), and imaging applications. Recently, the predicted performance of hollow-core photonic bandgap fibers (HC-PBGFs) shows the lowest loss (~0.1 dB/km) and the high speed (~98% of the velocity of light in free space) at 2-μm[2,3]. In addition, thulium-doped fiber amplifiers (TDFA) show high bandwidth operations in the 1.91-2.05 μm[4,5]. Therefore, the 2-μm communication band has been proposed to find the solution for the projected 'capacity crunch' of conventional single-mode fibers (SMFs) at 1.55-μm[6]. To develop this proposed communication band, various complementary metal-oxide-semiconductor (CMOS) Si-based optical devices such as low bending loss waveguide (WG)[7], micro-ring modulator[8],

 © xxxx IOP Publishing Ltd

Mach-Zehnder interferometer (MZI)[8], and four-mode division demultiplexer[9] operating at 2-µm have been reported. Moreover, another important photonic component, photodetectors (PDs) operating at 2-µm are essential[10]. Currently, III-V and II-VI materials are mainly used for designing the MIR PDs[11–15]. However, III-V and II-VI materials are not compatible with the current CMOS silicon (Si)-photonics technology.

In recent decades, the CMOS-compatible germanium-tin (GeSn) alloy shows promising material for silicon (Si)-based photonic devices, paving the path to the technological advancements in fiber-optic telecommunication, 5G, the internet of things (IoT), and light detection and ranging applications in short-wave infrared (SWIR) and MIR wavelength range[16–19]. Recently, several efforts have been made to design high-performance GeSn *p-i-n* PDs for 2000 nm bands[20–24]. However, the *trade-off* between the responsivity and 3dB bandwidth due to a thicker intrinsic layer limits its performance. Moreover, avalanche PDs have also been reported for 2000 nm bands[25] but they require high reverse-biased voltage (more than -1V) and also possess high noise which hampers the sensitivity of the device[26]. On the other hand, the common-emitter (C-E)-based three-terminals (3-Ts) phototransistors can provide extremely high responsivity (due to its internal current gain) and 3dB bandwidth while being biased with low voltages[27–29]. To this extent, in recent years a few research groups have focused on the design and fabrication of *vertical* bipolar junction transistor (BJT)-based GeSn heterojunction phototransistors (HPTs)[30–35]. Although, most of the earlier reported GeSn-based HPTs are designed for C- and L-bands of fiber-optic telecommunication[36][37]. Recently, our group has reported the GeSn-based HPTs for 2000 nm applications[38] but their 3dB frequency is not comparable with the GeSn *p-i-n* photodetectors[20]. However, the required high-performance HPTs (high responsivity and frequency response) are still not available for the 2000nm applications. Therefore, it is crucial to study and investigate the high-performance GeSn phototransistors for next-generation communication and sensing at 2000 nm.

In this work, we demonstrate a novel device structure; a *lateral* waveguide-based GeSn homojunction phototransistor (PTs), aiming for high responsivity and high 3dB bandwidth at the 2000 nm band. Lateral GeSn PTs on the Si platform is considered to meet the requirements of electronic-photonic integrated circuits (EPICs). In addition, our designed lateral GeSn PTs structure provides a better decoupling of photon absorption and photon-generated carrier path which enhances the optical gain of the device. Furthermore, lateral GeSn also enhances the optical confinement factor (OCF) in the intrinsic-GeSn layer, thereby, increasing the optical responsivity. The proposed device is simulated and its principle of operation is validated using finite element method (FEM) simulation and MATLAB tools. The designed devices are simulated at 2000 nm and exhibit optical gain (β_{op}) exceeding 1650 with the maximum responsivity of about 308A/W at $V_{BE} = 0.3V$ and $V_{CE} = 1V$. The proposed device also shows a significantly high 3dB bandwidth of about 55GHz at $V_{BE} = 0.3V$ and $V_{CE} = 1V$, which paves new opportunities for the design of next-generation high-speed monolithic photonic receivers.

2. Device Structure and Simulation

The three-dimensional (3-D) schematic of the proposed $Ge_{1-x}Sn_x$ (x = 6%) homojunction PTs is shown in Fig. 1(a) along with the direction of propagation of light. Fig. 1(b) shows the simulated band diagram of the designed device. In this structure, the light is launched to an *i*-GeSn waveguide, where it travels and is mostly absorbed by the PTs and then converted to photogenerated currents. The photon absorption length (L) is set to 10 µm, while the width of the path of the photogenerated carrier (W_i) will be optimized to get the highest performance. However, practically, the optical input signal is launched through a grating coupler[39] in waveguide-based PTs and it is absorbed by the PTs through evanescent wave coupling. The structural details and materials used for the proposed device are given in Table I. In this work, we have considered the GeSn thickness of 400 nm, which is well below the critical thickness[40]. Solid-source molecular beam epitaxy (MBE) can be used to grow the sample used in this study, which consists of (i) a 400-nm-thick *i*-GeSn active layer grown at 150°C and (ii) a high-quality, 600-nm-thick Ge strain-relaxed buffer (SRB) grown using two-step growth technique[41]. The Sn concentration and strain of the GeSn active layer can be determined by evaluating the structural characteristics of the generated sample using an x-ray diffraction approach[34]. Using CMOS-compatible fabrication techniques, the sample can then be fabricated into a planar waveguide *n-p-i-n* phototransistor with a waveguide structure. Reactive ion etching (RIE) followed by conventional optical lithography can be used to define a strip double mesa with a waveguide width of w between 100 and 900 nm. Following microwave annealing at 1650 W for 100s to activate the dopants, the *n*- and *p*-GeSn regions can then be created by ion-implantation P(B) at a 20 keV energy and a dosage of 10^{15} cm^2. Then, employing plasma-enhanced chemical vapor deposition (PECVD), a 300 nm thick SiO_2 passivation layer can be created. So, to expose the surface of the *n*-, *p*-, and *n*-GeSn regions, contact windows may be created utilizing RIE. In order to make electrical contact, Au/Cr electrodes with a thickness of 200/20 nm can then be deposited using an e-beam evaporator and patterned using lift-off procedures. To ensure mirror-like facets and reduce coupling loss, the fabricated samples will subsequently be precisely cleaved into devices along <100> directions.

The lattice mismatch between GeSn and Ge virtual substrate (VS) may cause high-density point dislocation at the heterointerfaces. The impact of defects (in terms of variation of hole diffusion length) on current gain, optical performance (responsivity, detectivity, and noise equivalent power), and

frequency performance (f_T and f_{MAX}) of vertical GeSn HPTs have been reported by Kumar et. al. [37,38]. Their results show that defects at the Ge/GeSn heterointerfaces have a significant impact on the current gain and frequency performance of HPT. However, the optical performance was less affected by the defects at the heterointerfaces. In the proposed lateral structure, the proximity to the Ge VS may also have a significant impact on the device performance depending on the stress. As a result, device current gain and frequency performance may be significantly affected. Therefore, in this work, for simplicity, we have considered unstrained Ge VS and the defect-free GeSn homojunction.

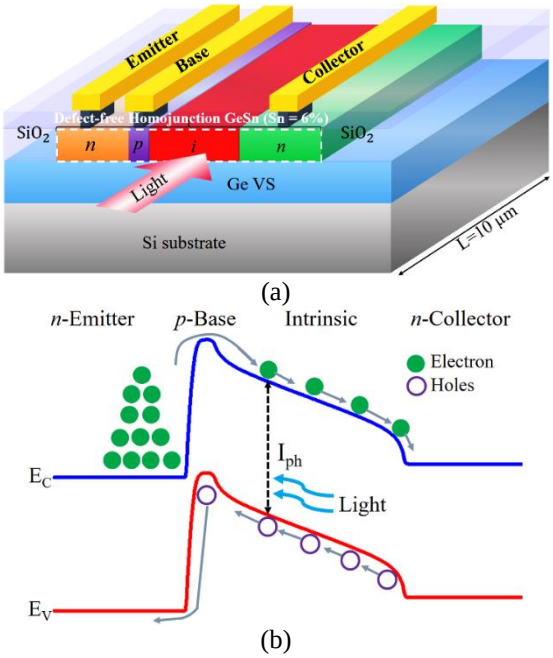

Fig. 1 (a)) Three-dimensional (3-D) schematic of the proposed lateral GeSn homojunction phototransistors, and (b) simulated band diagram of the proposed device under illumination.

In addition, in this work, as compared to conventional *n-p-n* BJT, *n-p-i-n* configuration has been considered, which results in lower collector doping. As a result, the base-collector (B-C) space-charge region widens, thereby widening the region where optically-generated electrons and holes are separated. The optically-generated electrons diffuse into the B-C space-charge region, where the built-in electric field will sweep the electron into the collector region, and the holes accumulate in the base region, where they control the intrinsic base-emitter (B-E) potential[42,43]. As a result of the change in the B-E potential, a large number of electrons injected from the emitter will diffuse across the base into the B-C depletion region and finally reach the collector region, considering that the base width is necessarily small to minimize recombination with any majority carrier holes in the base region. Therefore, the optical gain of PT can be calculated as[26],

$$G_{opt} = (I_C/q)/(P_{opt}/h\nu) \quad (1a)$$

$$G_{opt} = \beta \times \eta \quad (1b)$$

where G_{opt} and β are the common-emitter optical and electrical gain (in forward active mode[44,45]), respectively. I_C is the collector current, P_{opt} is the incident optical power, and $h\nu$ is the photon energy. q is the charge of the electron and η is the efficiency.

The GeSn material parameters such as bandgap energy, carriers' mobility, refractive index, and the density-of-states used in the simulation tool have been taken from[21,46,47] and their concrete values for x = 6% are given in Table II.A and B. The analytical expression to calculate bandgap energy is given as;

$$E_g^L(Ge_{1-x}Sn_x) = (1-x)E_g^L(Ge) + xE_g^L(Sn) - x(1-x)b_L \quad (1)$$

Where, $E_g^L(\mathrm{Ge_{1-x}Sn_x})$ represents the bandgap energy of $\mathrm{Ge_{1-x}Sn_x}$ alloy. $E_g^L(\mathrm{Ge}) = 0.664\,eV$ and $E_g^L(\mathrm{Sn}) = 0.092\,eV$ are the bandgap energy of pure Ge and Sn, respectively. $b_L = 0.89\,eV$ is the bowing parameter and x is the Sn concentration in $\mathrm{Ge_{1-x}Sn_x}$ alloy. Next, the carrier's mobility can be calculated using the following expressions;

$$\mu_e(\mathrm{Ge_{1-x}Sn_x}) = 3800 + 4456x \quad 2(a)$$

$$\mu_h(\mathrm{Ge_{1-x}Sn_x}) = 1800 + 33750x \quad 2(b)$$

Where, μ_e and μ_h are the electron and hole mobility, respectively.

TABLE I
STRUCTURAL DETAILS OF OUR PROPOSED GESN (SN = 6%)-BASED LATERAL HOMOJUNCTION PHOTOTRANSISTORS AT 300 K

Layer	Material	Width (in nm)	Doping (in cm^{-3})	Thickness (in nm)
n-Emitter (*n*-E)	$Ge_{1-x}Sn_x$	200-400	5×10^{19}	400 nm
p-Base (*p*-B)	$Ge_{1-x}Sn_x$	40-200	5×10^{18}	
i-Intrinsic (*i*)	$Ge_{1-x}Sn_x$	100-900	------	
n-Collector (C)	$Ge_{1-x}Sn_x$	300-500	5×10^{18}	
Virtual Substrate (VS)	Ge	------	------	600 nm
Substrate	Si	------	------	2000 nm

TABLE II.A
VALUES OF GESN (SN = 6%) MATERIAL PARAMETERS AT 300 K AT THE WAVELENGTH OF 2000 NM

Parameter	Values	Ref.
Bandgap energy (eV)	0.5795	[21]
Refractive index	$n = 4.3594$	[46]
	$k = 7.4799\times10^{-3}$	
Density-of-states (cm^{-3})	$N_C = 1.02\times10^{19}$	[47]
	$N_V = 2.38\times10^{18}$	

TABLE II.B
VALUES OF GESN (SN = 6%) MATERIAL PARAMETERS AT 300 K[21,48]

Regions	Mobility Values ($cm^2/V.s$)	
	μ_n	μ_p
n-GeSn (Emitter)	4067.36	114.51
p-GeSn (Base)	503.94	3825
i-GeSn (WG)	4067.36	3825
n-GeSn (Collector)	4067.36	340.09

To evaluate the optical confinement factor (OCF) and the normalized optical power through the *i*-GeSn waveguide, we have obtained various fundamental modes using the FEM simulations. This analysis also helps in determining the optimal *i*-GeSn waveguide width (W_i) to get the maximum 3dB frequency and responsivity of the device. The optical waveguide's performance is adversely affected by modal dispersion. The reduction of modal dispersion can be accomplished via single-mode optical waveguides. The proposed device structure has been designed in such a way that it does not support the higher-order waveguide modes. The structural details of the proposed device are given in the manuscript. The *i*–GeSn region (acts as a core, $n_{GeSn} = 4.3594$) is sandwiched between the upper clad layer (SiO_2, $n_{SiO_2} = 1.4381$) and lower the clad layer (Ge VS, $n_{Ge} = 4.1008$). Therefore, high refractive index contrast between the core and clad layers causes high optical confinement through the *i*-GeSn waveguide at λ=2000 nm. The power loss (also known as mode/propagation loss) related to the single optical mode depends on its imaginary part of the effective refractive index $\left(Im\left(n_{eff}\right)\right)$ and can be calculated by; $Loss\ (dB) = 10log_{10}(e) \cdot 4\pi Im\left(n_{eff}\right)/\lambda$, where, λ is the wavelength (in μm)[49]. The extinction coefficient (k, complex GeSn refractive index) is mainly responsible for the absorption coefficient of the GeSn material ($\alpha = 4\pi k/\lambda$)[50] and thus the responsivity of the device. The mode loss may considerably influence the performance of waveguide-based photonic devices, thus, large loss optical mode can't propagate in a waveguide. The proposed waveguide shows the loss of 0.16 dB for *i*-GeSn width and height of 500 nm and 400 nm, respectively. The extinction coefficient of 7.4799×10^{-3} results in the absorption coefficient 469.98/cm of GeSn material at λ = 2000 nm.

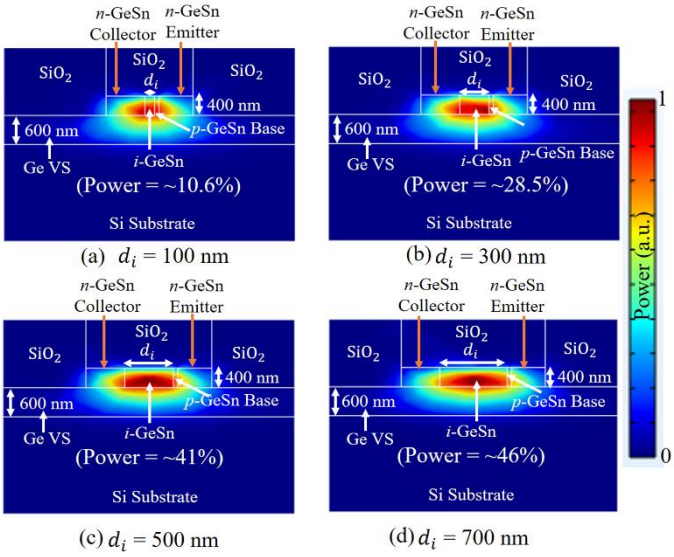

Fig. 2 Simulated energy distribution of quasi-transverse-electric field (fundamental mode) for different *i*-$Ge_{1-x}Sn_x$ (x = 6%) waveguide width.

In order to evaluate the normalized optical power, we have taken the ratio of integrated optical power in the *i*-GeSn waveguide over the integrated optical power through the complete device structure. The simulated quasi-transverse electric fundamental modes (TE_{00}) and the normalized optical power through the waveguide for different *i*-GeSn waveguide width (W_i) at an operating wavelength of 2000 nm is shown in Fig. 2. The result emphasizes that the quasi-transverse-electric field (E_x) confined mainly in the *i*-GeSn waveguide with the increase of W_i. In addition, the increase of W_i also leads to a significant enhancement in the normalized optical power through the *i*-GeSn waveguide. Therefore, the simulated result suggests larger *i*-GeSn width to get better OCF and the maximum optical power through the waveguide. However, wider *i*-GeSn width causes a poor frequency performance (in terms of 3dB bandwidth) of the proposed device. The impact of *i*-GeSn width on the 3dB bandwidth of the device is discussed in the next section.

3. Results and Discussion

In order to characterize the device's electrical and optical performance, we simulated the structure with an FEM simulator and analyzed the radio frequency response using MATLAB. In this work, all the analysis has been done at room temperature.

3.1 Gummel and output characteristics of phototransistors

Fig. 3(a) shows the simulated Gummel characteristics of the designed PT. The solid black curve is associated with terminal currents under the dark with $V_{CE} = 1V$. The key advantage of choosing $V_{CE} = 1$V may result in extremely low-power optical interconnect in order to be competitive[51]. The impact ionization (at $V_{CE} = 1V$) in the base-collector (B-C) space-charge region generates holes, neutralizing the forward base current and as a result, a base current reversal takes place. The result shows the ideal operation of the phototransistor. In Fig. 3(a) the dashed red curve shows the variation of terminal currents under illumination at λ=2000 nm. When light is coupled into the waveguide, the optical terminal currents follow the same curve of the transistor under dark. The optical absorption coefficient results in enhanced optical terminal currents compared to the electrically-biased transistor.

The simulated output characteristics (collector current *versus* V_{CE}) of the PTs under dark and illumination are shown in Fig. 3(b). The solid black curve represents the electrically-biased I_C as a function of V_{CE} for a fixed base current. The dashed red curve represents the optically-biased collector current (I_{Cop}) as a function of V_{CE} for a fixed optical power at λ=2000 nm. The characteristics noticeably reveal the transistor effect with an increase of the collector current with the incident optical power. The incident optical power input to the PTs is equivalent to the applied base current to the base terminal of the transistors. In addition, as a result of illumination, the photogenerated carriers modulate the base potential (usually the base potential decreases with the incident optical power) thus increasing the collector current[27,52].

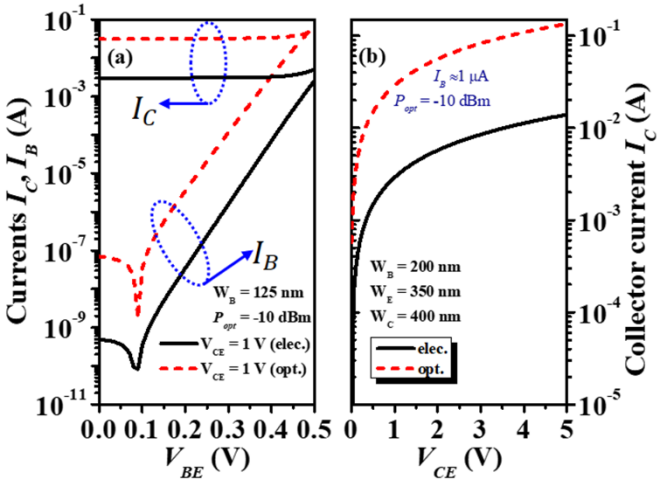

Fig. 3 Electrical and optical (a) Gummel and (b) output characteristics of the GeSn waveguide-based homojunction phototransistors.

The next important figure-of-merit is to compute the transistor gain with varying base-emitter voltage. Figure 4 demonstrates the calculated gain under dark and illumination (for a fixed optical power at λ=2000nm) as a function of base-emitter voltage The device exhibits relatively higher electrical current gain as compared with the optical gain. The relatively reduced optical is limited by two factors (i) efficiency[26] and (ii) increased recombination in the base-emitter space-charge region[53]. Mathematically, it can also be explained using Eqs. 1(a) and (b) [Section 2].;

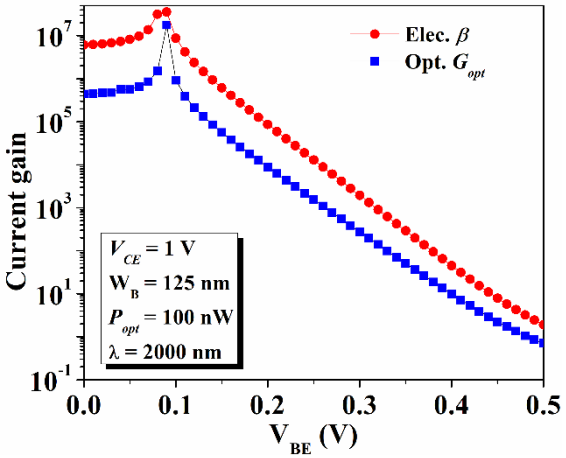

Fig. 4 Calculated current gain under dark and illumination (at λ= 2000 nm) as a function of applied base-emitter voltage for a constant $V_{CE} = 1V$.

In addition, it is observed that the optical and electrical current gain shows a peak value at ~0.1V. However, the optical current shows a sharp peak value compared to the electrical current gain. This is expected as we take into consideration the values of base current under illumination and dark. Generally, in phototransistors, the impact ionization in the B-C depletion region generates holes, neutralizing the base current and as a result, the base current dip occurs. Additionally, the optical absorption in the B-C region causes further base current reversal/dip under illumination[54]. Beyond $V_{BE} = 0.1V$, the electrical current starts dominating the photogenerated base current, thus, generating the sharp peak value of gain at $V_{BE} = 0.1V$. Moreover, the current gain starts decreasing beyond $V_{BE} = 0.1\,V$. This behavior can be explained based on the higher value of base current compared to the collector for larger values of V_{BE}. The increased base current/recombination current may be due to the (i)increased surface recombination velocity and (ii) widening of the base-emitter space-charge region. Similar behavior of current gain (strong dependence on V_{BE}) has also been reported earlier[53], which validates the presented result in this proposed work. The proposed PT exhibits sufficient gain between $0.1V \leq V_{BE} \leq 0.4V$. Therefore, $V_{BE} = 0.3V$ is chosen to be the optimal voltage to maintain the high gain and to analyze all the results.

3.2 Frequency response of phototransistors

Concerning the speed of the proposed PT, this is mainly limited by the forward transit time (consisting of both base transit time and base-collector transit time) and emitter charging time. Usually, the frequency response of the PTs is characterized by the 3dB bandwidth (f_T: the theoretical highest speed that a PT can achieve) and the maximum operating frequency at which a PT can operate (f_{MAX}). In this work, the *i*-GeSn region is fully depleted, therefore, base-collector junction capacitance ($C_{\mu op}$) due to both base-collector junction and intrinsic regions have been considered to calculate f_T and f_{MAX}. Therefore, the optimal base and *i*-GeSn region widths are desired to achieve high-speed PTs. The optimal *i*-GeSn width (d_i) can be achieved by estimating the normalized power bandwidth (NPBW) product. The theoretical model to calculate f_T and f_{MAX}under illumination has been taken from[55] and given as;

$$f_T = \frac{1}{2\pi\left(\left(\frac{V_T}{I_{Eop}}\right)(C_{\pi op}+C_{\mu op})+\tau_F\right)} \tag{3a}$$

$$f_{MAX} = \left(\frac{f_T}{8\pi C_{\mu op} R_{Bop}}\right)^{\frac{1}{2}} \tag{3b}$$

where V_T and I_{Eop} are the thermal voltage and emitter current, respectively. $C_{\pi op}$ and $C_{\mu op}$ are the capacitances due to base-emitter and base-collector junctions, respectively, and τ_F is the forward transit time. R_{Bop} is the base resistance under illumination. In this work, high base doping level and carriers' mobility yield low base resistance of ~37.9Ω. As a result, the proposed PT can operate at a higher frequency. The theoretical models to calculate the junction capacitances and forward transit time have been taken from[55] and given as;

$$C_{\pi op}=\frac{\epsilon_E A_E}{W_{BEop}} + \left(\frac{W_B^2}{2D_{nB}} + \frac{W_B}{v_s} + \frac{W_{BCop}}{2v_s}\right) g_{mop} \tag{4}$$

$$C_{\mu op}=\frac{L_E \epsilon_C}{W_{BCop}}(S_E + 2S_B) \tag{5}$$

$$\tau_F = \tau_B + \tau_{BC} = \frac{W_B^2}{2D_{nB}} + \frac{W_{BCop}}{2v_s} \tag{6}$$

where W_B is the base region width. W_{BCop} and W_{BEop} are the base-collector and base-emitter space-charge region widths, respectively. S_E and S_B are the width of the emitter and base stripe, respectively. ϵ_E and ϵ_C are permittivity of $Ge_{1-x}Sn_x$ (x = 6%), used in the emitter and collector regions, respectively. L_E and A_E are the length and cross-sectional area of the emitter

region. g_{mop} is the transconductance. D_{nB} and v_s are the minority electron diffusion constant in the base and saturation velocity of $Ge_{1-x}Sn_x$, respectively. The value of v_s for Sn = 6% has been taken from[56]. Here, the subscript '*op'* represents the parameters considered under illumination. The parameters used to calculate the values of 3dB bandwidth and maximum frequency of the proposed GeSn for a fixed *i*-GeSn layer width of 500 nm and base width of 45 nm is given in Table III.

TABLE III
CALCULATED VALUES OF PARAMETERS USED TO CALCULATE THE 3DB BANDWIDTH AND MAXIMUM FREQUENCY AT T = 300 K

Parameters	Value	Unit
$C_{\pi op}$	2.12	pF
$C_{\mu op}$	1.25	fF
τ_F	1.3	pS
S_E	350	nm
A_E	4×10^{-8}	cm^2
L_E	10	μm
S_B	45	nm
v_s	2×10^7	cm/s
R_{Bop}	37.9	Ω

Figure 5 shows the calculated 3dB bandwidth and maximum operating frequency of the designed PTs with varying base region width and *i*-GeSn waveguide width, respectively at $V_{BE} = 0.3V$ and $V_{CE} = 1V$. In addition, Fig. 5(b) also shows the variation of NPBW product versus waveguide width. The analysis shows that with the decrease in base region width and *i*-GeSn waveguide width, respectively, f_T increases due to the reduced forward transit time[30]. On the contrary, NPBW product initially increases with the decrease of *i*-GeSn width $(1000nm \leq d_i \leq 500nm)$ but later it starts decreasing for further decreasing *i*-GeSn width $(500nm \leq d_i \leq 100nm)$. The device shows the maximum values of NPBW product for $d_i = 500\ nm$. Next, the value of f_{MAX} is higher for lower base width, while in Fig. 5(d) it is higher for wider *i*-GeSn width. This behavior is expected as we take into the values of f_T and $C_{\mu op}$. Therefore, from the analysis, the optimal base width of 45nm and *i*-GeSn waveguide width of 500 nm has been considered for this work to achieve the desired frequency performance (high f_T and f_{MAX}) of the proposed PTs.

Table IV shows the value of 3dB bandwidth obtained from the proposed PT with the earlier reported waveguide-coupled Ge and *vertical* GeSn PTs. The comparison clearly shows that the GeSn PTs can not only achieve excellent performance at the new band $(2000\ nm)$ but also achieve better performance at 1.55 μm compared to reported Ge PTs. This high value of bandwidth obtained from the proposed device is attributed to the larger saturation velocity and high carriers' mobility of GeSn. The 3dB bandwidth of the PT was calculated to be >55 GHz for the optimal base region and *i*-GeSn waveguide width. Such excellent frequency performance is expected to make high-speed PTs for the next-generation 2000 nm optical communication.

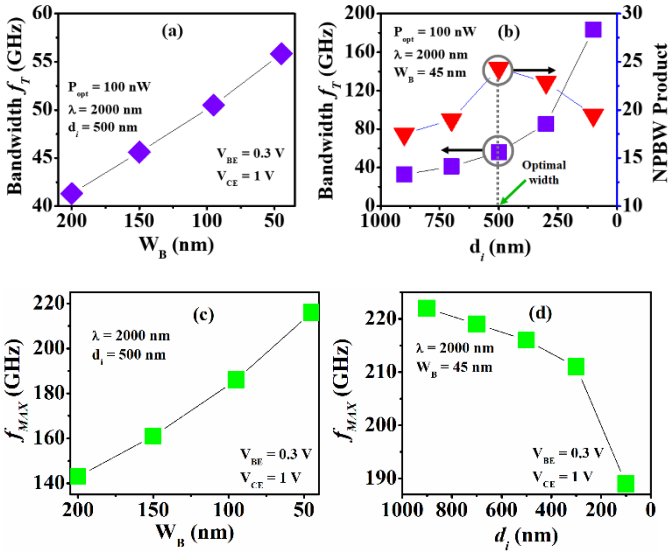

Fig. 5 Calculated 3dB bandwidth and maximum operating frequency with the scaling of the base layer and *i*-GeSn layer width. (a) and (c) f_T and f_{MAX} versus W_B for a fixed *i*-GeSn layer width of 500 nm, (b) f_T and normalized power in the waveguide and (d) f_{MAX} with the scaling of the intrinsic layer for a fixed base layer width of 45nm at λ=2000nm.

TABLE IV
COMPARATIVE VALUES OF BANDWIDTH OF WAVEGUIDE-COUPLED PTS

Waveguide-Coupled Device	Bandwidth (GHz)	Simulated /Measured	Ref.
Ge PT	10@1.55μm	Simulated	[26]
Ge PT	28@1.55μm	Simulated	[57]
Ge PT	14.5@1.55μm	Measured	[52]
Vertical-GeSn MQW PT	>18@1.55μm	Simulated	[58]
Vertical-GeSn (Sn = 6%)	42@1.55μm	Simulated	[30]
This Work	55@2μm	Simulated	------

3.3 Impact of lateral scaling on the gain of phototransistors

In general, the recombination factor and base transmission efficiency play a vital role in determining the current gain of the phototransistors. Therefore, the current gain strongly depends on the base layer width. The design considerations also suggest that the base layer width should be narrower compared to emitter and collector regions and it is defined as, $W_C > W_E > W_B$, where W_C, W_E, and W_B are the collector, emitter, and base widths, respectively[59]. Thus, in this section, the impact of lateral scaling of the base, emitter, and collector regions on the gain performance of PTs is taken into consideration. This analysis helps in choosing the optimal values of the base, collector, and emitter widths to achieve the maximum values of gain of PTs. The results are demonstrated in Fig. 6, which clearly shows that gain is strongly dependent on the base layer width. However, the gain is less dependent

on the emitter and collector region width. Specifically, the gain of PT decreases with the increase in base layer width. The reason is attributed to the increased recombination and decreased base transmission efficiency with the increasing base layer width[26]. Next, as the emitter width increases, the current gain increases slightly for $200\,nm \leq W_E \leq 350nm$ and then it decreases gradually for $350\,nm \leq W_E \leq 400nm$.This behavior can be explained based on a small enhancement in photogenerated current contribution in the collector region. Similarly, the increase of collector layer width results in a slight enhancement in the current gain of PT. However, the contribution of photogenerated current in the collector region is not significant as compared to the magnitude of photogenerated current in the absorption region[37]. As a result, the current gain is less dependent on the emitter and collector region widths, respectively. The impact of scaling on current gain for vertical GeSn-based HPTs has been reported earlier and their results showed similar trends, which validates the proposed work[37]. Thus, the optimal widths of the base, emitter, and collector region are determined to be 45nm, 350nm, and 400nm, respectively to maintain the high current gain (β_{op} ≈1650) and to calculate the responsivity of PT.

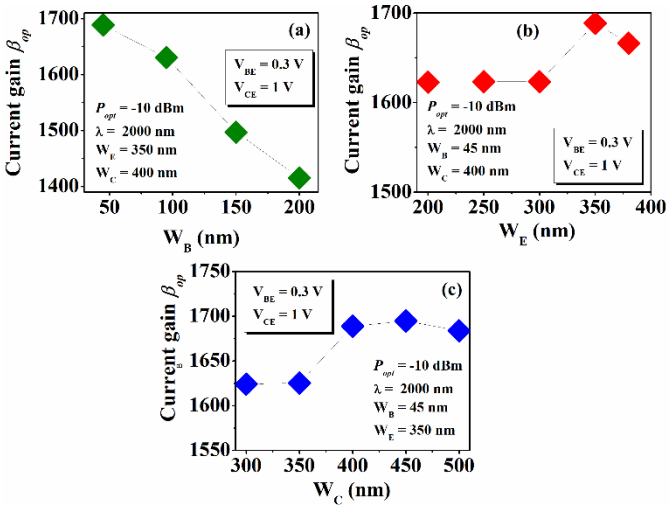

Fig. 6 Variation of current gain with (a) base width, (b) emitter width, and (c) collector width for $V_{BE} = 0.3\,V$ and $V_{CE} = 1\,V$ at λ= 2000 nm.

3.4 Analysis of responsivity of phototransistors

This section examines the most important metric the responsivity of PT with different bias conditions and incident optical power. In addition, we have also examined the I_{ON}/I_{OFF} ratio. The responsivity has been calculated using the relation, $R = I_{ph}/P_{opt} = (I_{Cop} - I_{C,dark})/P_{opt}$, where I_{ph} is the photogenerated current[27]. I_{Cop} and $I_{C,dark}$ are the collector current under illumination and dark, respectively, and P_{opt} is the incident optical power at λ = 2000nm . Next, the I_{ON}/I_{OFF} ratio can be calculated using the relation, I_{ON}/I_{OFF} (in dB) $= 20\lg[(I_{Cop} - I_{C,dark})/(I_{C,dark})]$[27]. Figure 7(a) demonstrates the calculated responsivity as a function of incident optical power with different collector-to-emitter voltage (V_{CE}) of 1V and 5V at λ = 2000nm. Fig. 7(b) and (c) shows the variation of I_{ON}/I_{OFF} and responsivity with collector-to-emitter voltage (V_{CE}) for a fixed value of V_{BE} = 0.3V at λ = 2000 nm. The result shows the strong dependence of responsivity on collector-to-emitter voltage. Specifically, responsivity increases significantly with increasing V_{CE}. This may be attributed to the increased photocurrent which is proportional to the square root of the exponential of V_{CE}. Next, as expected responsivity decreases significantly with the incident optical power (as shown in Fig. 7(a)). Such responsivity dependence on optical power is related to light affecting the base potential[60,61] and due to the low-doped GeSn base. With the increase in incident optical power, the generation rate in the base region increases significantly and the effective base doping level starts to increase as well. Since the gain of the transistor depends on the ratio of doping level between emitter and base ($gain \propto N_E/N_B$, where, N_E and N_B are the emitter and base doping level, respectively), so reducing this ratio would reduce the gain[52]. In addition, the effective increase in the base doping level would also decrease the base-width modulation effects. As a result, responsivity decreases with the incident optical power. Figure 7(b) illustrates the calculated I_{ON}/I_{OFF} ratio. This ratio explains the sensitivity of the device. The proposed PT exhibits high I_{ON}/I_{OFF} ratio of 20 dB at $V_{CE} = 1V$ for incident optical power of -10 dBm. This calculated result reveals the reduced dark current and the improved device sensitivity. The proposed PT achieves an excellent responsivity of 308 A/W with $V_{CE} = 1V$ for incident optical power of -10 dBm. The peak responsivity increases to ~1520A/W at $V_{CE} = 5V$, however, high bias voltages are not favored when the PT is used with advanced CMOS technologies, since there can be a huge mismatch in the DC voltage level. These responsivity values are based on simulations only and the fabricated device may show lower value than this. The reason may be attributed to the reduced absorption coefficient and current gain of the device. For example, the fabricated two-terminals GeSn PT with floating-base showed the theoretical value of responsivity of 155 A/W, however, its measured value was 1.8 A/W at λ=1550 nm[33].

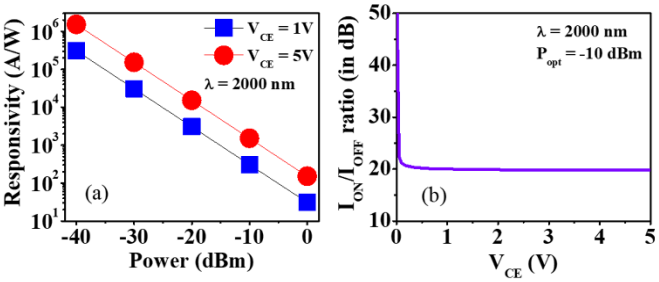

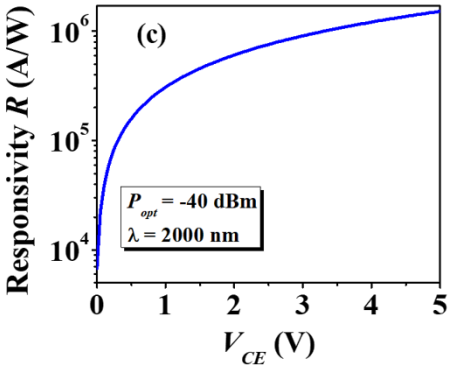

Fig. 7 (a) Simulated responsivity of PTs as a function of incident optical power with different collector-to-emitter voltage at λ = 2000 nm, (b) I_{ON}/I_{OFF} as a function of collector-to-emitter voltage at λ = 2000 nm, and (c) variation of responsivity with collector-to-emitter voltage at λ = 2000 nm at P_{opt} = -40 dBm.

3.5 Performance analysis: experimental mobility *vs* theoretical mobility

In this section, we predict the effect of experimental mobility on the performance of the proposed GeSn PT. Here, we have considered the experimental values of mobility for Sn = 4% (since the experimental values of Sn = 6% are not available). Theoretical mobility values for Sn = 4% were calculated using Eqs. 2(a-b). The experimental mobility values for GeSn, Ge, and Si were taken from[62–64]. The comparative analysis based on simulation is given in Table V. As expected, the device with experimental mobility exhibits about three times lower values of responsivity and bandwidth compared to the device with theoretical mobility. The reason is attributed to the reduced experimental mobility values compared to the theoretical mobility. Therefore, it can be predicted that devices with experimental values of mobility for Sn = 6% will show more or less a similar trend.

TABLE V
COMPARATIVE VALUES OF BANDWIDTH AND RESPONSIVITY WITH THEORETICAL AND EXPERIMENTAL VALUES OF MOBILITY AT $\lambda = 2000\,nm$, $P_{opt} = -40\,dBm$ WITH $V_{BE} = 0.3\,V$ AND $V_{CE} = 1V$

Parameters	GeSn (Sn = 4%) PT	
	With theoretical mobility	With experimental mobility
$R\ (A/W)$	3.43×10^5	1.04×10^5
$f_T\ (GHz)$	29.2	9.28

4. Conclusion

In conclusion, a high-performance lateral $Ge_{1-x}Sn_x$ (x = 6%) waveguide-based homojunction phototransistors on Ge-On-Si substrate have been presented. The Gummel and output characteristics under dark and illumination, the optical gain, and the responsivity of the PTs have been investigated using the FEM simulations. Furthermore, the frequency response has been analyzed using MATLAB. The proposed lateral device structure enables high optical confinement and power through the *i*-GeSn waveguide due to a better decoupling of photon absorption and photon-generated carrier path. As a result, a significant enhancement in the optical performance of the device has been observed. The simulated results show that the frequency performance and the current gain of the device were significantly affected by the increase in base width. On the contrary, the variation of emitter and collector widths have less impact on the current gain of the device. The discussion provided suggests a novel approach for designing high-performance phototransistors for extending the optical communication to the 2000nm region. The proposed device was simulated at λ=2000 nm and shows the maximum responsivity exceeding 1520 A/W 308A/W at V_{CE} =5V and 1V, respectively for P_{opt} = -10 dBm.

Acknowledgments

This work was supported in part by the National Research Foundation Singapore (NRF–CRP19–2017–01); Ministry of Education AcRF Tier 2 (T2EP50121- 0001 (MOE-000180-01)); Ministry of Education AcRF Tier 1 (2021-T1-002- 031 (RG112/21))

References

[1] Soref R 2015 Mid-infrared photonics *Optical Fiber Communication Conference, OFC 2015* (OSA Technical Digest (online) (Optical Society of America, 2015), paper W4A.4) pp 3–5

[2] Roberts P J, Couny F, Sabert H, Mangan B J, Williams D P, Farr L, Mason M W, Tomlinson A, Birks T A, Knight J C and St. J. Russell P 2005 Ultimate low loss of hollow-core photonic crystal fibres *Opt. Express* **13** 236

[3] Zhang H, Kavanagh N, Li Z, Zhao J, Ye N, Chen Y, Wheeler N V., Wooler J P, Hayes J R, Sandoghchi S R, Poletti F, Petrovich M N, Alam S U, Phelan R, O'Carroll J, Kelly B, Grüner-Nielsen L, Richardson D J, Corbett B and Garcia Gunning F C 2015 100 Gbit/s WDM transmission at 2 μm: transmission studies in both low-loss hollow core photonic bandgap fiber and solid core fiber *Opt. Express* **23** 4946

[4] Li Z, Heidt A M, Daniel J M O, Jung Y, Alam S U and Richardson D J 2013 Thulium-doped fiber amplifier for optical communications at 2μm *2013 Opt. Fiber Commun. Conf. Expo. Natl. Fiber Opt. Eng. Conf. OFC/NFOEC 2013* **21** 9289–97

[5] Li Z, Heidt A M, Simakov N, Jung Y, Daniel J M O, Alam S U and Richardson D J 2013 Diode-pumped wideband thulium-doped fiber amplifiers for optical communications in the 1800 – 2050 nm window *Opt. Express* **21** 26450

[6] Richardson D J 2010 Filling the light pipe *Science (80-.).* **330** 327–8

[7] Li J, Liu Y, Meng Y, Xu K, Du J, Wang F, He Z and Song Q 2018 2- μ m Wavelength Grating Coupler , Bent Waveguide, and Tunable Microring on Silicon Photonic MPW *IEEE Photonics Technol. Lett.* **30** 471–4

[8] Cao W, Hagan D, Thomson D J, Nedeljkovic M, Littlejohns C G, Knights A, Alam S-U, Wang J, Gardes F, Zhang W, Liu S, Li K, Rouifed M S, Xin G, Wang W, Wang H, Reed G T and Mashanovich G Z 2018 High-speed silicon modulators for the 2 μm wavelength band *Optica* **5** 1055–62

[9] Zheng S, Huang M, Cao X, Wang L, Ruan Z, Shen L and Wang J 2019 Silicon-based four-mode division multiplexing for chip-scale optical data transmission in the 2 μm waveband *Photonics Res.* **7** 1030–5

[10] Soref R 2015 Group IV photonics: Enabling 2 μm communications *Nat. Photonics* **9** 358–9

[11] Chen Y, Xie Z, Huang J, Deng Z and Chen B 2019 High-speed uni-traveling carrier photodiode for 2 μm wavelength application *Optica* **6** 884–9

[12] Wun J M, Wang Y W, Chen Y H, Bowers J E and Shi J W 2016 GaSb-Based p-i-n Photodiodes with Partially Depleted Absorbers for High-Speed and High-Power Performance at 2.5-μm Wavelength *IEEE Trans. Electron Devices* **63** 2796–801

[13] Yang H, Ye N, Phelan R, O'Carroll J, Kelly B, Han W, Wang X, Nudds N, MacSuibhne N, Gunning F, O'Brien P, Peters F H and Corbett B 2013 Butterfly packaged high-speed and low leakage InGaAs quantum well photodiode for 2000nm wavelength systems *Electron. Lett.* **49** 293–5

[14] Refaat T F, Abedin M N, Sulima O V., Singh U N and Ismail S 2004 Novel infrared phototransistors for atmospheric CO2 profiling at 2 μm wavelength *Technical Digest - International Electron Devices Meeting, IEDM* pp 355–8

[15] Refaat T F, Abedin M N, Sulima O V., Ismail S and Singh U N 2004 AlGaAsSb/InGaAsSb phototransistors for 2-μm remote sensing applications *Opt. Eng.* **43** 1647–50

[16] Dominici S, Wen H, Bertazzi F, Goano M and Bellotti E 2016 Numerical study on the optical and carrier recombination processes in GeSn alloy for E-SWIR and MWIR optoelectronic applications *Opt. Express* **24** 26363–81

[17] Dascalescu I, Zoita N C, Slav A, Matei E, Iftimie S, Comanescu F, Lepadatu A M, Palade C, Lazanu S, Buca D, Teodorescu V S, Ciurea M L, Braic M and Stoica T 2020 Epitaxial GeSn Obtained by High Power Impulse Magnetron Sputtering and the Heterojunction with Embedded GeSn Nanocrystals for Shortwave Infrared Detection *ACS Appl. Mater. Interfaces* **12** 33879–86

[18] Kong Z, Wang G, Liang R, Su J, Xun M, Miao Y, Gu S, Li J, Cao K, Lin H, Li B, Ren Y, Li J, Xu J and Radamson H H 2022 Growth and Strain Modulation of GeSn Alloys for Photonic and Electronic Applications *Nanomaterials* **12** 1–15

[19] Du W and Yu S Q 2019 *Group IV photonics using (Si)GeSn technology toward mid-IR applications* (Elsevier Ltd.)

[20] Kumar H and Pandey A K 2022 GeSn-Based Multiple-Quantum-Well Photodetectors for Mid-Infrared Sensing Applications *IEEE Trans. Nanobioscience* **21** 175–83

[21] Kumar H and Basu R 2022 Design of Mid-Infrared Ge1-xSnx Homojunction p-i-n Photodiodes on Si Substrate *IEEE Sens. J.* **22** 7743–51

[22] Dong Y, Wang W, Xu S, Lei D, Gong X, Guo X, Wang H, Lee S-Y, Loke W-K, Yoon S-F and Yeo Y-C 2017 Two-micron-wavelength germanium-tin photodiodes with low dark current and gigahertz bandwidth *Opt. Express* **25** 15818–27

[23] Tsai C-H, Lin K-C, Cheng C-Y, Lee K-C, Cheng H H and Chang G-E 2021 GeSn lateral p-i-n waveguide photodetectors for mid-infrared integrated photonics *Opt. Lett.* **46** 864–7

[24] Zhou H, Xu S, Lin Y, Huang Y-C, Son B, Chen Q, Guo X, Lee K H, Goh S C-K, Gong X and Tan C S 2020 High-efficiency GeSn/Ge multiple-quantum-well photodetectors with photon-trapping microstructures operating at 2 μm *Opt. Express* **28** 10280–93

[25] Chen Q, Wu S, Zhang L, Fan W and Tan C S 2021 Simulation of High-Efficiency Resonant-Cavity-Enhanced GeSn Single-Photon Avalanche Photodiodes for Sensing and Optical Quantum Applications *IEEE Sens. J.* **21** 14789–98

[26] Frounchi M, Tzintzarov G N, Ildefonso A and Cressler J D 2021 High Responsivity Ge Phototransistor in Commercial CMOS Si-Photonics Platform for Monolithic Optoelectronic Receivers *IEEE Electron Device Lett.* **42** 196–9

[27] Sorianello V, De Angelis G, De Iacovo A, Colace L, Faralli S and Romagnoli M 2015 High responsivity SiGe heterojunction phototransistor on silicon photonics platform *Opt. Express* **23** 28163–9

[28] Kamitsuna H, Matsuoka Y, Yamahata S and Shigekawa N 2000 A 82-GHz-optical-gain-cutoff-frequency InP/InGaAs double-hetero-structure phototransistor (DHPT) and its application to a 40-GHz-band OEMMIC photoreceiver *2000 30th European Microwave Conference, EuMC 2000* (Paris, France: IEEE)

[29] Tegegne Z 2016 *SiGe/Si Microwave Photonic devices and Interconnects towards Silicon-based full Optical Links* (Univ. Paris-Est, Champs-sur-Marne, France, May 2016)

[30] Kumar H and Basu R 2019 Effect of Active Layer Scaling on the Performance of Ge 1– x Sn x Phototransistors *IEEE Trans. Electron Devices* **66** 3867–73

[31] Kumar H, Basu R and Gupta J 2019 Small-Signal Compact Circuit Modeling of Group IV Material-Based Heterojunction Phototransistors for Optoelectronic Receivers *IEEE Trans. Electron Devices* **66** 1797–803

[32] Kumar H and Basu R 2018 Noise Analysis of Group IV Material-Based Heterojunction Phototransistor for Fiber-Optic Telecommunication Networks *IEEE Sens. J.* **18** 9180–7

[33] Wang W, Dong Y, Lee S-Y, Loke W-K, Lei D, Yoon S-F, Liang G, Gong X and Yeo Y-C 2017 Floating-base germanium-tin heterojunction phototransistor for high-efficiency photodetection in short-wave infrared range *Opt. Express* **25** 18502–7

[34] Hung W-T, Barshilia D, Basu R, Cheng H H and Chang G-E 2020 Silicon-based high-responsivity GeSn short-wave infrared heterojunction phototransistors with a floating base *Opt. Lett.* **45** 1088–91

[35] Kumar H 2021 High-speed short-wave infrared Si-based GeSn MQW phototransistor: An alternative to existing photodetectors *Semicond. Sci. Technol.* **36**

[36] Pandey A K, Basu R and Chang G-E 2018 Optimized Ge1-xSnx/Ge Multiple-Quantum-Well Heterojunction Phototransistors for High-Performance SWIR Photodetection *IEEE Sens. J.* **18** 5842–52

[37] Pandey A K, Basu R, Kumar H and Chang G E 2019 Comprehensive Analysis and Optimal Design of Ge/GeSn/Ge p-n-p Infrared Heterojunction Phototransistors *IEEE J. Electron Devices Soc.* **7** 118–26

[38] Kumar H and Basu R 2021 Effect of Defects on the Performance of Si-Based GeSn/Ge Mid-Infrared Phototransistors *IEEE Sens. J.* **21** 5975–82

[39] Wang Y, Flueckiger J, Lin C and Chrostowski L 2013 Universal grating coupler design *Photonics North 2013* vol 8915 (Ottawa, Canada: SPIE) p 89150Y

[40] Wang W, Zhou Q, Dong Y, Tok E S and Yeo Y C 2015 Critical thickness for strain relaxation of Ge1-xSnx ($x \leq 0.17$) grown by molecular beam epitaxy on Ge(001) *Appl. Phys. Lett.* **106** 232106(1-5)

[41] Tseng H H, Li H, Mashanov V, Yang Y J, Cheng H H, Chang G E, Soref R A and Sun G 2013 GeSn-based p-i-n photodiodes with strained active layer on a Si wafer *Appl. Phys. Lett.* **103** 1907(1-5)

[42] Chand N, Houston P A and Robson P N 1985 Gain of a Heterojunction Bipolar Phototransistor *IEEE Trans. Electron Devices* **32** 622–7

[43] Moriizumi T and Takahashi K 1972 Theoretical Analysis of Heterojunction Phototransistors *IEEE Trans. Electron Devices* **19** 152–9

[44] Chang C Y, Wu B S, Fang Y K and Lee R H 1985 Optical and Electrical Current Gain in an Amorphous Silicon Bulk Barrier Phototransistor *IEEE Electron Device Lett.* **6** 149–50

[45] Campbell J C 1985 Phototransistors for Lightwave Communications *Semiconductors and Semimetals* vol 22 pp 389–447

[46] Tran H, Du W, Ghetmiri S A, Mosleh A, Sun G, Soref R A, Margetis J, Tolle J, Li B, Naseem H A and Yu S-Q 2016 Systematic study of Ge1-xSnx absorption coefficient and refractive index for the device applications of Si-based optoelectronics *J. Appl. Phys.* **119** 103106(1-9)

[47] Song Z, Fan W, Tan C S, Wang Q, Nam D, Zhang D H and Sun G 2019 Band structure of Ge1-xSnx alloy: A full-zone 30-band k • p model *New J. Phys.* **21** 073037(1-11)

[48] Chang G E, Yu S Q, Liu J, Cheng H H, Soref R A and Sun G 2022 Achievable Performance of Uncooled Homojunction GeSn Mid-Infrared Photodetectors *IEEE J. Sel. Top. Quantum Electron.* **28** 3800611(1-11)

[49] Huang H, Liu K, Qi B and Sorger V J 2016 Re-analysis of single-mode conditions for silicon rib waveguides at 1550 nm wavelength *J. Light. Technol.* **34** 3811–7

[50] Zhu S, Chen T P, Cen Z H, Goh E S M, Yu S F, Liu Y C and Liu Y 2010 Split of surface plasmon resonance of gold nanoparticles on silicon substrate: a study of dielectric functions *Opt. Express* **18** 21926–31

[51] Assefa S, Xia F, Green W M J, Schow C L, Rylyakov A V and Vlasov Y A 2010 CMOS-integrated optical receivers for on-chip interconnects *IEEE J. Sel. Top. Quantum Electron.* **16** 1376–85

[52] Going R, Seok T J, Loo J, Hsu K and Wu M C 2015 Germanium wrap-around photodetectors on Silicon photonics *Opt. Express* **23** 11975–84

[53] Krishnakumar K S, Dinesh C M, Ramani ., Khan S A and Kanjilal D 2012 60 and 100 MeV oxygen ion irradiation effects on electrical characteristics of bipolar transistor *16th International Workshop on Physics of Semiconductor Devices* vol 8549 p 85490M

[54] Pandey A K, Basu R, Kumar H and Chang G E 2019 Comprehensive Analysis and Optimal Design of Ge/GeSn/Ge p-n-p Infrared Heterojunction Phototransistors *IEEE J. Electron Devices Soc.* **7** 2–6

[55] Kumar H, Basu R and Chang G E 2020 Impact of Temperature and Doping on the Performance of Ge/Ge1-xSnx/Ge Heterojunction Phototransistors *IEEE Photonics J.* **12** 6801814(1-14)

[56] Ghosh S, Bansal R, Sun G, Soref R A and Cheng H 2022 Design and Optimization of GeSn Waveguide Photodetectors for 2- μ m Band Silicon Photonics *Sensors* **22** 3978(1-20)

[57] Going R 2015 *Ultra-low energy photoreceivers for optical interconnects* (UC Berkeley, Berkeley, CA, USA)

[58] Kumar H 2021 High-speed short-wave infrared Si-based GeSn MQW phototransistor: An alternative to existing photodetectors *Semicond. Sci. Technol.* **36** 065023(1-8)

[59] Sze S M and Ng K K 2017 *Physics of Semiconductor Devices* (Hoboken, New Jersey, United States: John Wiley & Sons, Inc.)

[60] Ang K W, Yu M Bin, Lo G Q and Kwong D L 2008 Low-voltage and high-responsivity germanium bipolar phototransistor for optical detections in the near-infrared regime *IEEE Electron Device Lett.* **29** 1124–7

[61] Kostov P, Gaberl W, Hofbauer M and Zimmermann H 2012 PNP PIN bipolar phototransistors for high-speed applications built in a 180 nm CMOS process *Solid. State. Electron.* **74** 49–57

[62] Tao P, Tang W, Wang Y, Shi J, Cheng H H and Wu X 2020 Optoelectronic properties for the compressively strained Ge1-xSnx films grown on Ge(004) *Mater. Res. Express* **7** 035902(1-9)

[63] Nakatsuka O, Tsutsui N, Shimura Y, Takeuchi S, Sakai A and Zaima S 2010 Mobility behavior of Ge1-xSnx layers grown on silicon-on-insulator substrates *Jpn. J. Appl. Phys.* **49** 04DA10(1-4)

[64] Tobehn-Steinhäuser I, Reiche M, Schmelz M, Stolz R, Fröhlich T and Ortlepp T 2021 Carrier Mobility in Semiconductors at Very Low Temperatures *The 8th International Symposium on Sensor Science* pp 86(1-5)